Available online at www.sciencedirect.com
SCIENCE DIRECT®
International Journal of Heat and Fluid Flow 27 (2006) 21–32
International Journal of HEAT AND FLUID FLOW
www.elsevier.com/locate/ijhff

Experimental study on flow and local heat/mass transfer characteristics inside corrugated duct

Sang Dong Hwang, In Hyuk Jang, Hyung Hee Cho *

Department of Mechanical Engineering, Yonsei University, 134, Shinchon-dong, Seodaemun-gu, Seoul 120-749, Republic of Korea

Received 30 September 2004; received in revised form 13 June 2005; accepted 4 July 2005
Available online 19 September 2005

Abstract

The present study investigates the flow and heat/mass transfer characteristics of wavy duct for the primary surface heat exchanger application. Local heat/mass transfer coefficients on the corrugated duct side walls are measured using a naphthalene sublimation technique. The flow visualization technique and a numerical analysis using a commercial code, FLUENT, are used to understand the overall flow structures inside the duct. The corrugation angle of the wavy duct is 145° and the duct aspect ratio is 7.3. The Reynolds numbers, based on the duct hydraulic diameter, vary from 100 to 5000. The results show that complex secondary flows and transfer processes exist inside the wavy duct resulting in non-uniform distributions of the heat/mass transfer coefficients on the duct side walls. At low Reynolds numbers ($Re \leqslant 1000$), relatively high heat/mass transfer regions like cell shapes appear on both pressure- and suction-side walls due to the secondary vortex flows called Taylor–Görtler vortices perpendicular to the main flow direction. However, at high Reynolds numbers ($Re > 1000$), these secondary flow cells disappear and boundary layer type flow develop on pressure-side wall. On the suction-side wall, high heat/mass transfer region appears by the flow reattachment. The average heat/mass transfer coefficients are higher than those of the smooth circular duct and pressure drop increases due to the secondary flows inside wavy duct.

Keywords: Corrugated duct; Taylor–Görtler vortex; Primary surface heat exchanger; Naphthalene sublimation technique; Flow visualization

1. Introduction

In general, power plants and micro turbine systems are designed to obtain high effectiveness and low pressure losses, minimum volume and weight, and high reliability and low cost (McDonald and Wilson, 1996). For gas turbine recuperators, an efficient heat exchanger is required to reduce size and increase cycle efficiency. And in these applications, generally the heat exchangers contain flow channels with various cross-sectional shapes, and corrugated, curved or wavy in the main flow direction, to enhance the heat/mass transfer rates. Several investigations have shown that secondary flows perpendicular to the streamwise flow direction are induced by the shape of the corrugated or wavy duct. These secondary flow motions distort the main flows and enhance the overall heat transfer coefficients. However, the pressure loss increases and non-uniform heat transfer distributions are induced.

Various numerical studies and approaches to the flow and heat transfer characteristics in corrugated or wavy ducts are conducted. Asako and Faghri (1987) conducted the numerical studies to predict heat transfer coefficients, friction factors, and streamlines of the corrugated duct at laminar flow region (Reynolds numbers range from 100 to 1500). Sawyers et al. (1998) investigated steady laminar heat transfer characteristics in corrugated channels using a combination of analytical and numerical techniques. Rokni and Sunden (1998), and

* Corresponding author. Tel.: +82 2 2123 2828; fax: +82 2 312 2159.
E-mail address: hhcho@yonsei.ac.kr (H.H. Cho).

0142-727X/$ - see front matter © 2005 Elsevier Inc. All rights reserved.
doi:10.1016/j.ijheatfluidflow.2005.07.001

Nomenclature

A	naphthalene-coated surface area
D_h	hydraulic diameter
D_{naph}	naphthalene vapor diffusivity in air
dy_N	naphthalene sublimation depth
f	friction factor in Eq. (6)
f_0	friction factor for smooth pipe
H	duct height
H/W	aspect ratio
h_m	mass transfer coefficient
L	duct length
$\dot{m}$	mass transfer rate per unit area
Nu	Nusselt number
n	exponent in Eq. (5)
P	corrugation pitch
Pr	Prandtl number
Re	Reynolds number
Sc	Schmidt number
Sh	Sherwood number
Sh_0	Sherwood number of smooth pipe
Sh_{avg}	overall average Sherwood number in Eq. (4)
$Sh_{avg,span}$	span average Sherwood number in Eq. (3)
U	average duct inlet velocity
W	duct width
x	streamwise coordinate (Fig. 1)
y	distance from the center in Fig. 1
z	spanwise coordinate (Fig. 1)
ΔP	pressure drop per unit length
P.F.	performance factor in Eq. (7)

Subscripts

laminar	based on laminar flow
turbulent	based on turbulent flow

Greeks

α	corrugation angle
ρ_{air}	density of the air
ρ_s	density of solid naphthalene
$\rho_{v,\infty}$	naphthalene vapor density of the air
$\rho_{v,w}$	naphthalene vapor density on the surface
dt	time interval during experiment

Rokni and Gatski (2001) conducted numerical calculations of convective heat transfer coefficients in trapezoidal ducts. They found that enhancement of heat transfer and increase in pressure losses were obtained by changes of duct shape. Utriainen and Sunden (2000) calculated the flow and heat transfer performance of a primary surface type heat exchanger and presented Nusselt numbers and friction factors in a wavy duct. They compared the results with corresponding results of straight ducts for various cross-sectional shapes.

Many experimental studies about heat/mass transfer characteristics of straight ducts have been conducted. For example, Cho et al. (2003) investigate flow and local heat/mass transfer characteristics of a rectangular duct with rib turbulators. For the wavy duct, Goldstein and Sparrow (1977) investigated the overall heat/mass transfer characteristics for flow in a corrugated wall channel with an aspect ratio of 42.5 using naphthalene sublimation technique. The Reynolds number varied from 500 to 3100 in their experiments. They concluded that complex secondary flows and transfer processes exist resulting in heat/mass transfer augmentation at low Reynolds number. As a successive study, O'Brien and Sparrow (1982) carried out heat transfer measurements to determine the convective heat transfer coefficients. They measured friction factors in a corrugated duct with a corrugation angle of 30° and an aspect ratio of 10. Sparrow and Comb (1983) investigated the effects of inlet conditions of a corrugated wall heat exchanger. Nishimura et al. (1990) studied the detailed flow structures for various sinusoidal wavy channels using a flow visualization technique and found the occurrence of Taylor–Görtler vortices due to the flow instabilities. Recently, Islamoglu and Parmaksizoglu (2003) examined the effects of two different channel heights on heat transfer and friction characteristics of a corrugated channel, and concluded that the fully developed Nusselt number increases as channel height increases. They also performed a numerical study using finite element methods for the corrugated heat exchanger channel and the results are compared with the experimental results (Islamoglu and Parmaksizoglu, 2004).

Many numerical studies have been conducted; however, most have not confirmed the validity of assumptions included in their calculations due to the shortage of verified experimental data. For the experimental studies, most researches deal with the flow and average heat transfer characteristics of wavy ducts, but not with the local heat/mass transfer characteristics. The present study focuses on measurements of the detailed local mass transfer coefficients in wavy ducts having a rectangular cross-section for application to compact heat exchangers. In this study, the effects of the flow velocity on the local heat/mass transfer in corrugated duct are investigated. The flow patterns are examined by a flow visualization technique and a numerical analysis using the commercial code, FLUENT. Local mass transfer coefficients on the corrugated walls are measured using a naphthalene sublimation technique. The Reynolds numbers, based on the duct hydraulic diameter, vary from 1000 to 5000. The tested corrugation angle (α) and aspect ratio (H/W) of the wavy duct are 145° and 7.3, respectively.

2. Experimental apparatus and procedures

2.1. Experimental apparatus

Fig. 1 shows a schematic view of the experimental apparatus that consists of a blower, an orifice flowmeter, a plenum chamber and a test section. Room air entrained from the inlet contraction flows through the test duct and the plenum chamber then is discharged out of the room by the blower (3.7 kW). Flow rates are measured using a thin plate orifice flowmeter installed between the plenum chamber and the blower. The temperatures of the flow and room air are measured by the thermocouples (J-type). The geometry and coordinate system of the test section are shown in Fig. 1(b). The corrugated duct consists of ten pairs of pressure-side and suction-side walls. Hence, the total length of the wavy duct is five-corrugation pitches and the test section is located at the fourth pitch from the inlet contraction. The duct has sharp-edged turns and a rectangular cross-section. The aspect ratio and corrugation angle of the wavy duct are 7.3 and 145°, respectively. The corrugation pitch (P) between the turning edges is 64.0 mm. The detailed dimensions and hydraulic diameter of the wavy ducts are described in Table 1.

Flow visualization is applied to understand the overall flow structures inside the wavy duct using direct smoke injection method. The smoke tracers generated by the smoke generator are supplied to the test duct. An argon-ion laser (DANTEC, 5W) and a cylindrical lens is applied to produce a bright two-dimensional light sheet for taking instantaneous pictures, and the path lines are captured by a digital camera (Nikon Coolpix 990). The path lines formed by the flowing smoke particles provide information of the flow field in the wavy duct.

Table 1
Dimensions of wavy duct

Duct height (H)	53.0 mm
Duct width (W)	7.3 mm
Aspect ratio (H/W)	7.3
Duct length (L)	33.5 mm
Hydraulic diameter (D_h)	12.8 mm
Corrugation angle (α)	145°

Mass transfer experiments using a naphthalene sublimation method are conducted instead of the heat transfer experiments so that local transfer characteristics on the duct side walls are determined. Mass transfer experiments using the naphthalene sublimation method have some advantages, such as eliminating the conduction and radiation errors, and obtaining detailed local transfer coefficients. The mass transfer coefficients can be converted to heat transfer coefficients using the heat and mass transfer analogy. For the mass transfer experiments, four pieces of test plate are installed on each side wall (each pressure-side and suction-side wall). In order to obtain the local mass transfer coefficients, the profile of the naphthalene-coated surface on the test plate is scanned by an automated surface measuring system before and after exposure to the flow. The sublimation depth during the experiment is calculated from the difference of the surface profiles. The surface profile measuring and scanning system consists of an LVDT

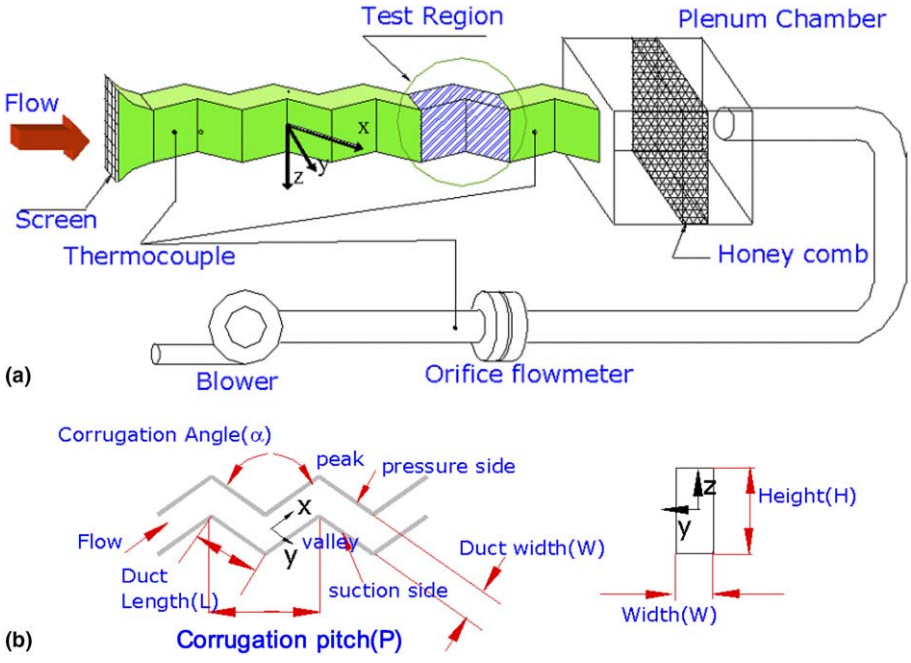

Fig. 1. Schematic view of experimental apparatus: (a) schematic diagram of experimental setup, (b) details of test section.

(Linear Variable Differential Transformer; LB-375TA-020), a traverse system, a digital multimeter and a GPIB board. Details of the measuring system and procedures are presented by Cho and Rhee (2001).

Five pressure taps having 1.0 mm in diameter holes are installed at $x/(P/2) = 0$ on the bottom wall of the duct to measure the pressure drop through the duct. The spacing between pressure taps is the same as the corrugation pitch (P). The static pressure is measured using a digital micromanometer (FCO-510) with the accuracy of 0.001 mm H_2O.

2.2. Numerical analysis

A numerical analysis using the commercial program (FLUENT) is performed in order to understand the flow patterns inside wavy duct. The computational domain is modeled by the same geometry used in the experiment and the operating conditions are equal to those of the experiments. To reduce grid sizes and calculation times, the periodic boundary condition is applied to the inlet and outlet of the flow. The computational grid is generated by grid generation program, GAMBIT(V2.1.6), and the number of grids is about 250,000.

In the numerical calculation, two calculation models, a laminar flow model and a turbulent flow model, are used because the Reynolds numbers based on the duct's hydraulic diameter and the flow velocity vary from 500 to 3000. For flows of Reynolds number below 1000, a steady laminar flow model is used. For Reynolds numbers over 1000, a turbulent model of RNG k–ε is applied with a standard wall function for near wall treatment.

Fig. 2 shows the computational domain and view planes used in the numerical calculation. In Fig. 2, stream-center (SC) plane indicates the center plane along streamwise directions ($z/(P/2) = 0$), and span-center (PC) plane is the spanwise center plane between the flow inlet and outlet planes ($x/(P/2) = 0$). The span-1(P-1) and span-2(P-2) planes are the spanwise planes located in the middle of the flow inlet and span-center ($x/(P/2) = -0.525$), and the span-center and flow outlet planes ($x/(P/2) = 0.525$), respectively.

2.3. Heat/mass transfer coefficients

The local mass transfer coefficient is defined as

$$h_m = \frac{\dot{m}}{\rho_{v,w} - \rho_{v,\infty}} = \frac{\rho_s(dy_N/d\tau)}{\rho_{v,w}} \tag{1}$$

Since the environmental air entrained to the test section contains no naphthalene vapor, the naphthalene density of the inlet air is zero ($\rho_{v,\infty} = 0$) in the present study. Therefore, the mass transfer coefficient is calculated from the local sublimation depth of the naphthalene (dy_N), run time (dt), density of the solid naphthalene (ρ_s), and the naphthalene vapor density ($\rho_{v,w}$). The naphthalene vapor pressure is obtained from a correlation of Ambrose et al. (1975). Then, the naphthalene vapor density, $\rho_{v,w}$, is calculated from the perfect gas law.

The Sherwood number can be expressed as

$$Sh = \frac{h_m D_h}{D_{naph}} \tag{2}$$

D_{naph} is the naphthalene vapor diffusivity in the air based on the discussion of naphthalene properties given by Goldstein and Cho (1995).

The span averaged Sherwood number and overall averaged Sherwood number are obtained by numerical integration:

$$Sh_{avg,span} = \left[\frac{\int_{-H/2}^{H/2} Sh\, dz}{\int_{-H/2}^{H/2} dz}\right]_x \tag{3}$$

$$Sh_{avg} = \frac{\int_0^L \int_{-H/2}^{H/2} Sh\, dz\, dx}{A} = \frac{\int_0^L \int_{-H/2}^{H/2} Sh\, dz\, dx}{LH} \tag{4}$$

where A is the naphthalene-coated surface area of each side wall.

The mass transfer coefficients can be converted to heat transfer coefficients using the heat and mass transfer analogy (Eckert, 1976).

$$\frac{Nu}{Sh} = \left(\frac{Pr}{Sc}\right)^n \tag{5}$$

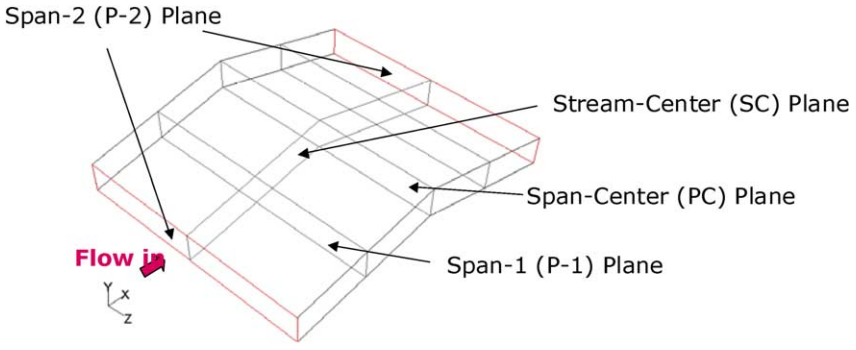

Fig. 2. Shape of the wavy duct and view planes used in numerical calculation.

The exponent n is the constant determined from the empirical results and depends on the flow conditions. In this study, the exact value of n for this flow type is not known with certainty for this flow and the straight channel flow and the wavy channel flow are not expected to have the same n value. The detailed discussions for the exponent, n, are presented by Eckert (1976), and Goldstein and Cho (1995).

Uncertainty of the Sherwood number using Kline and McClintock's method (1953) for the single sample experiments is within 7.2% in the entire operating range of the measurements, based on a 95% confidence level. This uncertainty is attributed mainly to the uncertainty of properties of the naphthalene, such as the naphthalene saturated vapor pressure (5.1%), and diffusion coefficient of the naphthalene vapor in the air (3.0%).

2.4. Pressure drop

The fanning friction factor, f, is defined as

$$f = \frac{\Delta P}{4(1/D_h)(1/2)\rho_{air}U^2} = \frac{1}{2}\Delta P\frac{D_h}{\rho_{air}U^2} \tag{6}$$

where ΔP, ρ_{air} and U indicate the pressure drop per unit length, the density of the air and the average velocity at duct inlet, respectively. The friction factor is obtained by linearly fitting the slope of pressure drop through the wavy duct.

The performance factor, P.F., is obtained by considering both heat/mass transfer enhancement and the friction loss increase based on the constant pumping power condition, and defined as

$$\text{P.F.} = \frac{Sh/Sh_0}{(f/f_0)^{1/3}} \tag{7}$$

where Sh_0 is the Sherwood number of smooth circular duct and f_0 is a friction factor of smooth circular duct. For laminar flow, Sh_0 and f_0 of a laminar analysis result for smooth circular pipe are applied. For turbulent flow, experimental correlations of Sh_0 of smooth circular duct presented by Dittus and Boelter (1985), and f_0 of smooth circular duct presented by Bhatti and Shah (1987) are applied.

3. Results and discussion

3.1. Flow characteristics

The flow patterns inside corrugated duct by smoke flow visualization are shown in Fig. 3. Fig. 3(a) illustrates the view planes and the directions of laser sheets. At $Re = 500$ (Fig. 3(b)), the main flow slightly deflects to the pressure-side wall due to the existence of the turning region. A small recirculation bubble is formed at the valley region of the duct. Flow separation and reattachment appear at the opposite wall to the valley. These flow patterns appear periodically through the wavy duct. For the front view (spanwise flow pattern), secondary vortices perpendicular to the streamwise direction are observed. The secondary vortices (secondary flow cells) are formed due to the centrifugal instability caused by the shape of the corrugated duct. These vortices are considered to be the Taylor–Görtler vortex kind which appeared on concave surfaces. At the end-wall region, small vortices are observed. It is considered that these vortices are generated by the secondary flow cells generated at the center region induced by the centrifugal instabilities. For $Re = 1000$ (Fig. 3(c)), the main flow is deflected to the pressure-side wall and weak secondary flow cells are also observed at the spanwise plane. But at a relatively high Reynolds number ($Re = 3000$), these secondary flow cells vanish because the flow becomes turbulent. It is considered that these secondary flows promote transition from laminar to turbulent flow.

Fig. 4 shows numerical calculation results of velocity contours with increasing flow Reynolds numbers from 100 to 3000. At low Reynolds number ($Re = 100$), the main flow flows through the wavy duct and is deflected to the pressure-side wall. At $Re = 700$ (Fig. 4(b)), the secondary flows as shown in flow visualization results are observed due to the curvature of the wavy duct, but these vortices vanish at a relatively high Reynolds number of 3000. The overall trends of the numerical calculation are consistent with the flow visualization results. However the onset of secondary flow cells is at $Re = 700$ in the numerical simulation results while the secondary vortex flow cells appear at $Re = 500$ in the flow visualization results. For the flow visualization result at $Re = 1000$, the strength of the secondary flows is also weaker than that of the numerical calculation. For the numerical calculation results, the occurrence of secondary vortices is more downstream of the experimental results. This is possibly due to the differences between the numerical simulation and experimental setup, because the test apparatus has more flow disturbances than those of numerical calculation.

Fig. 5 shows a schematic flow patterns in the streamwise and spanwise directions based on the flow visualization and numerical calculation results. As explained above, the streamwise flows are disturbed at the turning corner showing recirculation flow and flow separation/reattachment. The main core flow is deflected to the pressure-side wall due to the flow inertia force. The flow separation and reattachment occurs weakly at the peak corner. The secondary vortices perpendicular to the streamwise direction have two vortex patterns; one is the Taylor–Görtler type secondary vortex appearing in the middle region and the other is an array of the corner vortices as affected by the end-wall. The Taylor–Görtler

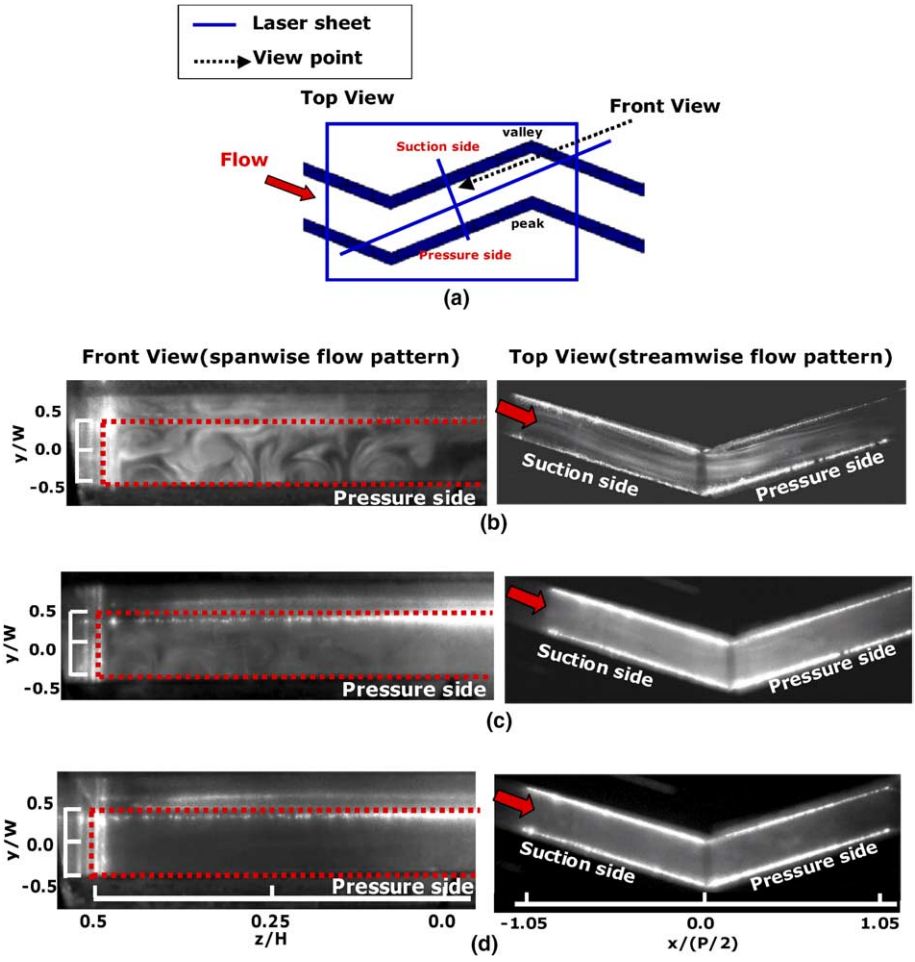

Fig. 3. Smoke flow visualization results: (a) view point, (b) $Re = 500$, (c) $Re = 1000$, (d) $Re = 3000$.

vortex region has several counter-rotating secondary vortex cells. The counter-rotating vortex pairs impinge on the downward flow region and are detached from the upward flow region on the pressure-side wall. On the suction-side wall, the separation/reattachment flows influence the secondary vortex flows. At the end-wall affected region, the corner vortices, which are normally observed at the corner of a non-circular duct, are formed near the top and bottom end-walls. Hence, the heat/mass transfer characteristics on the duct wall are affected strongly by these secondary vortex flow characteristics in the wavy duct.

3.2. Mass transfer characteristics

Fig. 6 presents contour plots of the Sherwood numbers on both pressure-side and suction-side walls for various Reynolds numbers with the corrugation angle of 145°. The "x" and "z" coordinates represent the streamwise and spanwise direction, respectively. At the low Reynolds number of 300, the Sherwood number has peak values at $z/(P/2) \cong \pm 0.5$, ± 0.2 and $x/(P/2) \cong 0.2$ on the pressure-side wall. These peaks are generated by the secondary vortex flows as shown in the flow visualization. As explained before, the downward and upward flows are formed in the secondary vortex cells (Taylor–Görtler vortices). The downward flow on the pressure-side wall enhances the mass transfer due to the impingement effects at $z/(P/2) \cong \pm 0.5$, ± 0.2 and $x/(P/2) \cong 0.2$. On the contrary, relatively low mass transfer regions appears at the location of $z/(P/2) \cong 0.0$, ± 0.3 and $x/(P/2) \cong 0.6$ due to the upward flow. At the corner region ($z/(P/2) \cong \pm 0.8$), high mass transfer regions appear due to the side walls. As Reynolds number increases to 500, the effects of the secondary flows increase and high mass transfer regions like cell-shape appear clearly. And overall Sherwood numbers increase due to the increased flow velocity. When Reynolds number is 1000, the effects of the secondary flows become weak on the pressure-side wall except in the end-wall region. It is because Taylor–Görtler vortex is vanishing as the flow transitions to turbulent as the flow velocity increases. On the suction-side wall, by the effect of the transitional secondary flows, high mass transfer regions

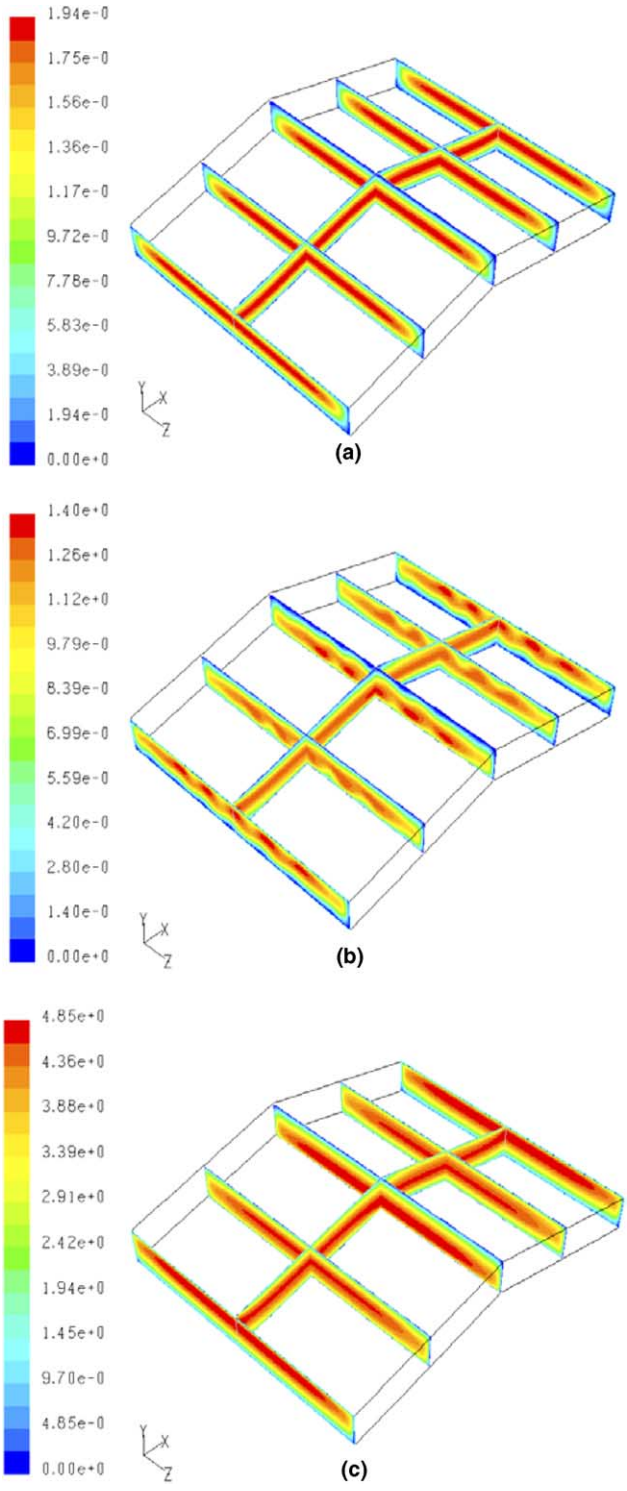

Fig. 4. Velocity contour plots with increasing Re at each spanwise and streamwise plane: (a) $Re = 100$, (b) $Re = 700$, (c) $Re = 3000$.

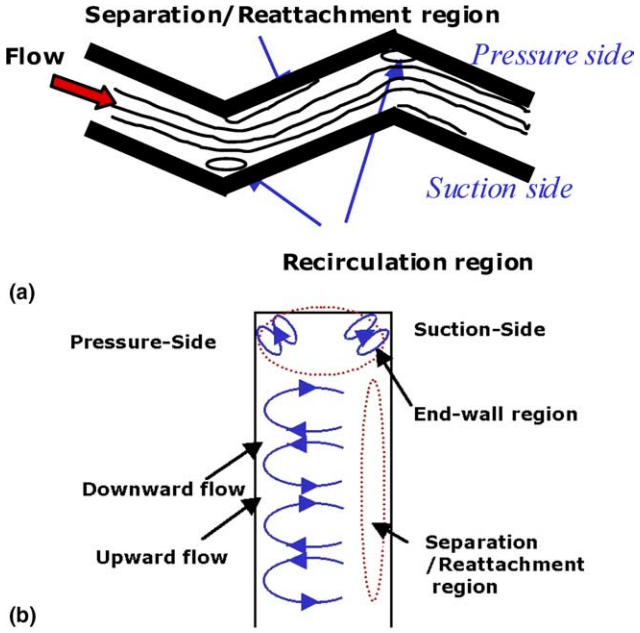

Fig. 5. Schematic flow patterns: (a) streamwise flow pattern, (b) spanwise flow pattern.

appear. At $Re = 1500$, high mass transfer regions due to the secondary flows vanished. Therefore Sherwood number distributions are relatively uniform along the spanwise direction, except at the end-wall region ($z/(P/2) \cong \pm 0.8$), but the Sherwood number decreases along the streamwise direction on the pressure-side due to boundary layer development of the duct flow. At $Re = 3000$, the Sherwood number decreases along the streamwise direction on the pressure-side wall but a high mass transfer region of $-0.6 < z/(P/2) < 0.6$ and $0.2 < x/(P/2) < 0.4$ appears due to the reattachment of separated flow at the edge of the duct turning on the suction-side wall. For $Re = 5000$, overall Sherwood number distributions are similar to those of $Re = 3000$ and Sherwood number values increase due to the increased Reynolds number.

Figs. 7 and 8 show local Sherwood number plots at $x/(P/2) = 0.19$, 0.42, 0.61 and 0.80 at $Re = 500$ and $Re = 3000$. At the low Reynolds number of 500 (Fig. 7), local peaks in Sherwood number appear at $z/(P/2) \cong \pm 0.2$, ± 0.5 and ± 0.7 due to the secondary flow on the pressure side. On the suction side, local peaks appear though the peak values are lower than those on the pressure side. When the Reynolds number is 3000 (Fig. 8), relatively uniform Sherwood number distributions appear, except in the end-wall regions on both the pressure-side and the suction-side walls. At this Reynolds number of 3000, the effects of Taylor–Görtler vortices vanish and Sherwood number has high values at the inlet region of $x/(P/2) = 0.19$ on the pressure side. On the suction side, due to flow separation/reattachment, high Sherwood number values appear at $x/(P/2) = 0.19$ and decrease gradually along the streamwise direction.

Fig. 9 shows the comparisons of the Sherwood number distributions with increasing Reynolds number on each pressure-side and suction-side wall at

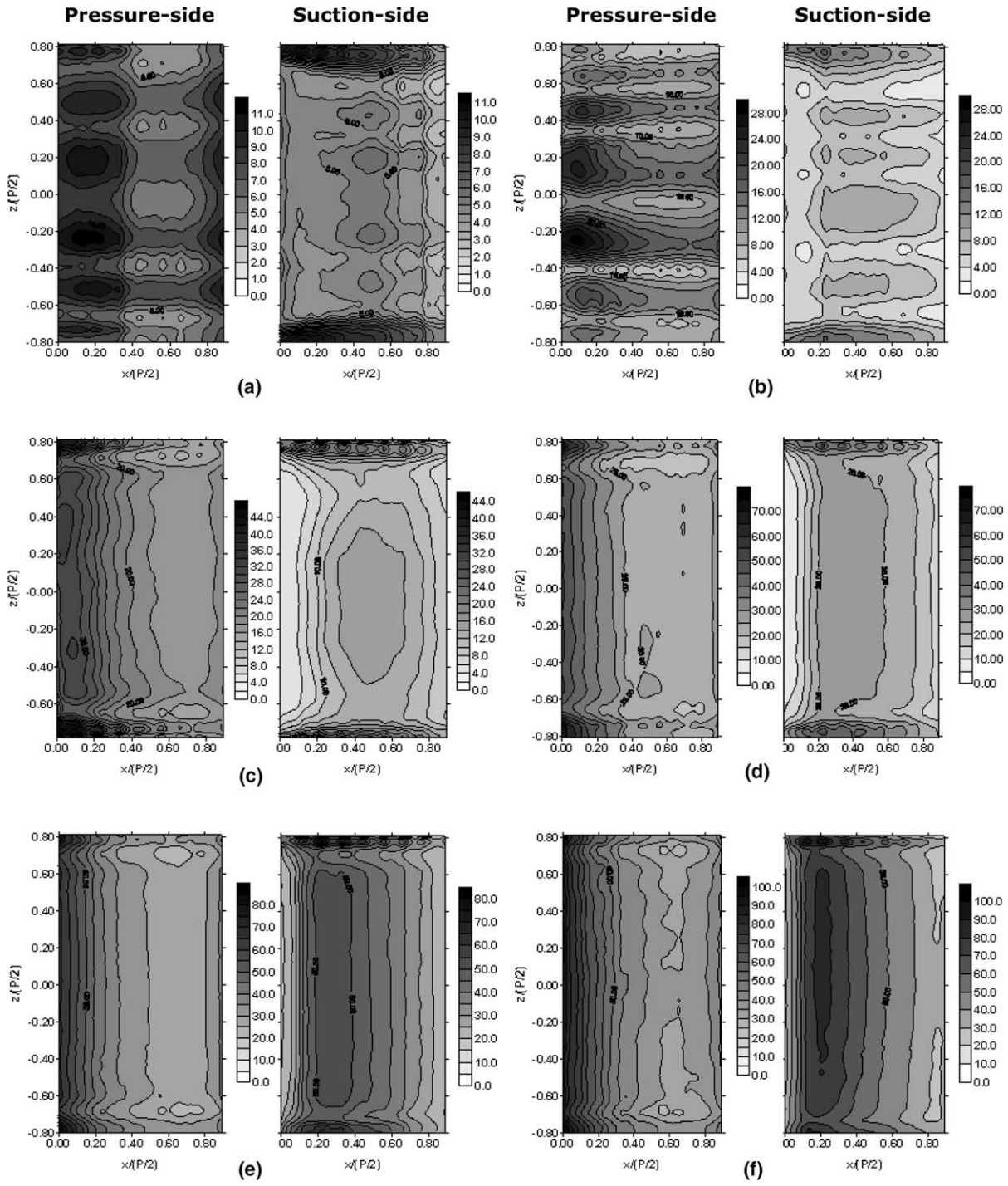

Fig. 6. Contour plots of *Sh* with increasing *Re*: (a) $Re = 300$, (b) $Re = 500$, (c) $Re = 1000$, (d) $Re = 1500$, (e) $Re = 3000$, (f) $Re = 5000$.

$x/(P/2) = 0.19$. At the low Reynolds number ($Re \leqslant 1000$), local peak values in Sherwood number exist at $z/(P/2) \cong \pm 0.2$ and ± 0.5 due to the downward flow. Relatively low Sherwood number values appear at $z/(P/2) \cong 0$, ± 0.4 and ± 0.6 due to the upward flow on the pressure side. On the suction side, non-uniform Sherwood number distributions appear due to the secondary flows. At high Reynolds numbers ($Re \geqslant 1000$), the effects of secondary flow cells disappear and uniform Sherwood number distributions appear along the spanwise direction except in the corner regions on the pressure side. On the suction-side wall, uniform distributions in Sherwood number appear and the Sherwood number values are a slightly higher than those on the pressure-side wall because a flow reattachment region is formed at $x/(P/2) \cong 0.19$.

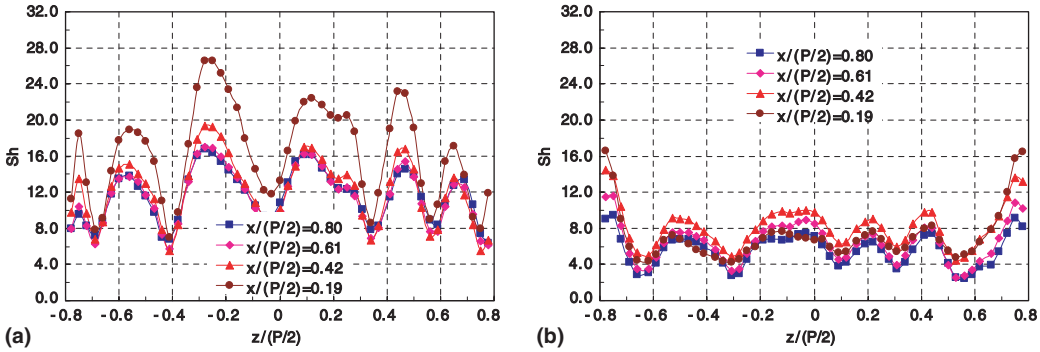

Fig. 7. Local *Sh* plots at $x/(P/2) = 0.19$, 0.42, 0.61 and 0.80 at $Re = 500$: (a) pressure side, (b) suction side.

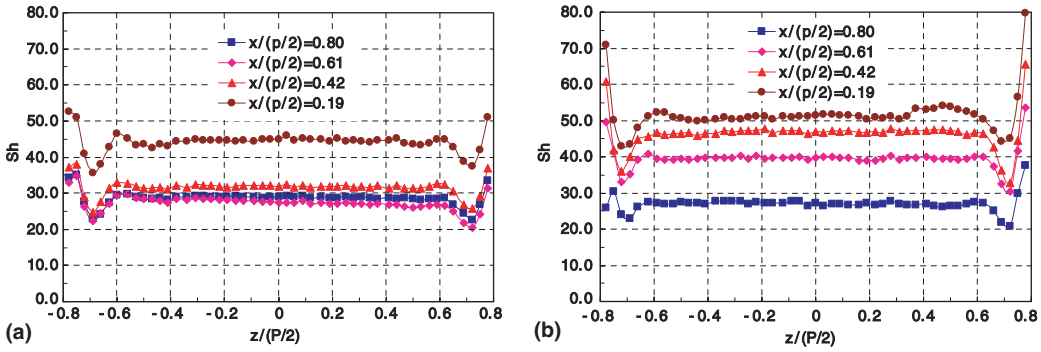

Fig. 8. Local *Sh* plots at $x/(P/2) = 0.19$, 0.42, 0.61 and 0.80 at $Re = 3000$: (a) pressure side, (b) suction side.

Fig. 10 shows the span average Sherwood number distributions with increasing Reynolds number. The streamwise coordinate, $x/(P/2)$ below about 1.0 means pressure-side wall and above 1.0 indicates suction-side wall. At the low Reynolds number ($Re \leqslant 1000$), on the pressure side, high span average Sherwood number values appear at $x/(P/2) \cong 0.2$ due to the existence of high mass transfer regions that correspond to the cell shapes induced by the secondary vortex flows, and the Sherwood numbers decrease gradually in the streamwise direction. On the suction side, low span average Sherwood number values appear at $x/(P/2) \cong 1.2$ because low mass transfer regions by secondary flow cells exist as shown in Fig. 6. However, span average Sherwood numbers increase a little at the region of $x/(P/2) \cong 1.4$ due to the secondary flows effects, then decrease gradually in the streamwise direction. At the high Reynolds number ($Re \geqslant 1000$), span average Sherwood number values decrease gradually in the streamwise direction because the secondary vortex flows vanished and boundary layer type flow develops on the pressure side. High span average Sherwood number values exist at $x/(P/2) \cong 1.2$ due to reattachment of the separated flow on the suction side. After flow reattachment, span average Sherwood number values decrease gradually in the streamwise direction due to the boundary layer development.

3.3. Average mass transfer, pressure drop and performance factor

Fig. 11 shows the average Sherwood number and normalized Sherwood number distributions for various Reynolds numbers. $Sh_{0,\text{laminar}}$ and $Sh_{0,\text{turbulent}}$ indicate the compared Sherwood number values of smooth circular pipe for laminar flow and turbulent flow respectively. The average Sherwood numbers increase linearly with increasing Reynolds number. At $Re \leqslant 3000$, the average Sherwood number values on the pressure-side wall are higher than those on the suction-side wall. It is because at low Reynolds number, Taylor–Görtler vortices are generated, resulting in enhanced mass transfer. And these secondary vortices strongly affect the mass transfer on the pressure-side wall. But at high Reynolds number ($Re \geqslant 3000$), the average Sherwood number values on suction side are higher than those on the pressure side due to reattachment of the separated flow. For the normalized Sherwood number distributions (Fig. 11(b)), values increase with increasing flow velocity and are about five times those of a smooth circular pipe at $Re \leqslant 1000$. This is because the secondary flow cells exist and the intensities of the secondary flows increase with increasing Reynolds number, resulting in enhanced mass transfer at low Reynolds numbers. But with $Re \geqslant 1000$, the effects of the Taylor–Görtler vortices vanish and the

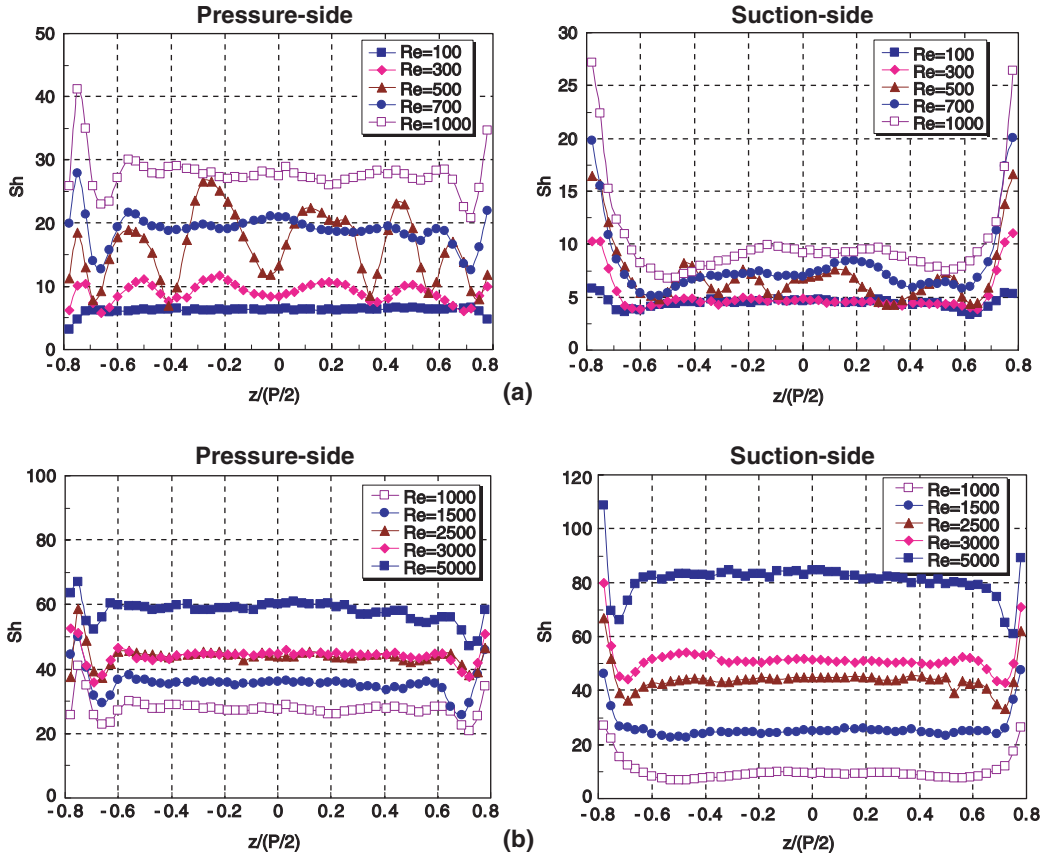

Fig. 9. *Sh* distribution with increasing *Re* at $x/(P/2) = 0.19$: (a) low *Re* ($Re \leqslant 1000$), (b) high *Re* ($Re \geqslant 1000$).

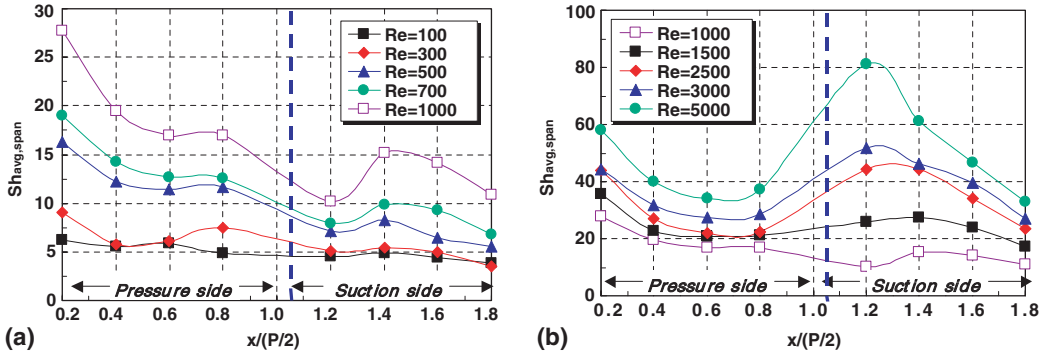

Fig. 10. Span average *Sh* distribution with increasing *Re*: (a) low *Re* ($Re \leqslant 1000$), (b) high *Re* ($Re \geqslant 1000$).

effects of flow separation and reattachment become dominant. Hence, the normalized Sherwood number values maintain a relatively uniform value of 2.

Fig. 12 shows the friction factor and normalized friction factor distributions for various Reynolds numbers. The compared $f_{0,\text{laminar}}$ and $f_{0,\text{turbulent}}$ also indicate the friction factor of smooth circular pipe by a laminar analysis and the friction factor of turbulent flow presented by Bhatti and Shah (1987), respectively. The friction factors of the wavy duct are about two to four times those of the smooth pipe. At Reynolds numbers below 1000, normalized friction factors increase with increasing Reynolds number. This is because, as explained above, the secondary flow cells are generated and the intensities of these vortex cells increase with Reynolds number resulting in increasing pressure losses at low Reynolds number. At the Reynolds numbers above 1000, the friction factors are about three times those of a smooth pipe and maintain relatively uniform values with increasing Reynolds numbers.

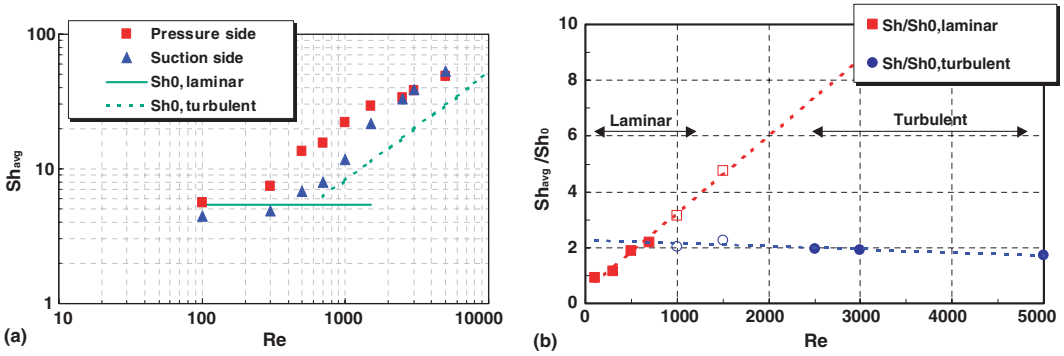

Fig. 11. Average *Sh* and normalized *Sh* distribution for various *Re*: (a) average *Sh*, (b) normalized *Sh*.

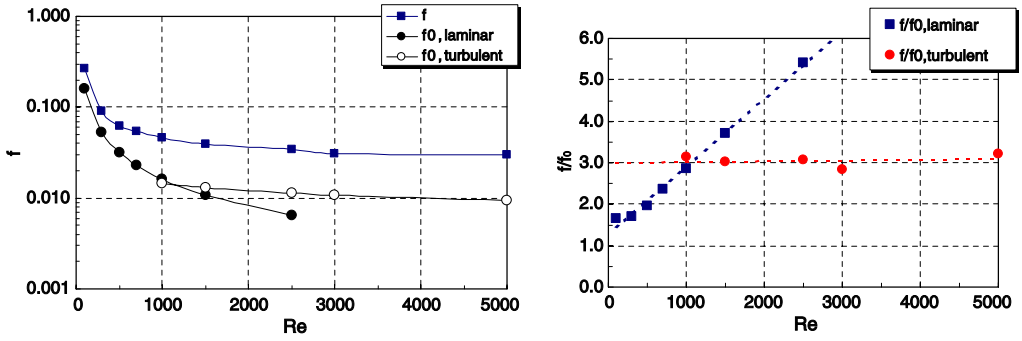

Fig. 12. Friction factor and normalized friction factor distribution for various *Re*: (a) friction factor, (b) normalized friction factor.

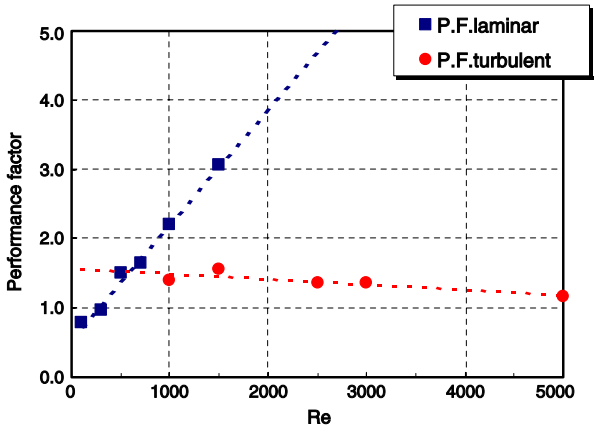

Fig. 13. Performance factor distribution.

Fig. 13 shows the performance factor distributions. At $Re \leqslant 1000$, the performance factors, which are based on the laminar analysis, increase with increasing Reynolds number. At this low Reynolds number range, mass transfer is enhanced and also pressure drop increases due to the secondary flows. However mass transfer enhancements are relatively higher than increases of pressure drop, therefore the performance factors have larger values than 1.0 except that for the low Reynolds number of 100. But the performance factor decreases gradually with Reynolds number for $Re \geqslant 1000$. It is because the Taylor–Görtler vortices are vanishing and flow separation/reattachment characteristics occur after the Reynolds number of 1000. Hence, the amount of pressure drop increase is relatively higher than that of mass transfer enhancement.

4. Conclusions

In this study, the flow and local mass transfer characteristics inside corrugated duct applied as a primary surface type heat exchanger are investigated. Local mass transfer coefficients on the corrugated duct side walls are determined using a naphthalene sublimation technique. The flow visualization technique and a numerical analysis using a commercial code, FLUENT, are used to understand the overall flow structures inside the duct. The principal conclusions of the present study are summarized as follows:

(1) *Flow and mass transfer characteristics*: At low Reynolds number ($Re \leqslant 1000$), the secondary vortices perpendicular to the streamwise direction are generated inside the duct. These secondary vortices are the Taylor–Görtler vortex type and are due to flow instability induced by curvature of the wavy duct. By these secondary

flows, non-uniform mass transfer coefficient distributions occur on the duct side walls. High Sherwood number regions are formed on duct walls due to the Taylor–Görtler vortex flow. But at high Reynolds numbers ($Re \geqslant 1000$), the effects of the secondary Taylor–Görtler vortex flows disappear as the flow transitions from laminar to turbulent flow. On the pressure-side wall, relatively uniform Sherwood number distributions along spanwise direction appear, except in the end-wall regions and boundary layer type flow characteristics are observed. On the suction-side wall, high mass transfer regions appear due to the flow separation and reattachment.

(2) *Average mass transfer*: The average mass transfer increases with increasing Reynolds number. The average Sherwood number values on the pressure-side wall are higher than those on the suction-side wall due to the strong effects of the Taylor–Görtler vortices at $Re \leqslant 3000$. But at high Reynolds numbers ($Re \geqslant 3000$), the average Sherwood number values on the suction side are higher than those on the pressure side due to the reattachment of the separated flow.

At $Re = 1000$, the average Sherwood number values are about five times those of a smooth circular pipe due to the occurrence of the secondary flow cells. At high Reynolds numbers ($Re \geqslant 1000$), the average Sherwood number values are about two times those of a smooth circular pipe because of the effects of flow separation and reattachment.

(3) *Pressure drop*: For the wavy duct, the pressure drop is higher than that of smooth circular pipe. The friction factors of wavy duct are about two to four times those of the smooth pipe. At $Re \leqslant 1000$, the friction factor increases with increasing Reynolds number due to the generation and development of the secondary flow cells resulting in increasing pressure losses. At $Re \geqslant 1000$, the friction factors are about three times those of a smooth pipe and maintain relatively uniform values.

(4) *Performance factor*: For the wavy duct, high performance factors of 2.2 are obtained at a low Reynolds number of 1000 due to relatively higher mass transfer enhancement than increase pressure loss. But the performance factor decreases gradually at $Re \geqslant 1000$ because the secondary vortices disappear and flow separation/reattachment flow characteristics occur.

Acknowledgements

This work was supported by the National Research Laboratory program of KISTEP (Korea Institute of Science and Technology Evaluation and Planning) and also carried out as a part of the Next-Generation New Technology Development Program "Development of High Efficiency Gas Turbine/Fuel Cell Hybrid Power Generation System", which is supported by Ministry of Commerce, Industry and Energy, Korea.

References

Ambrose, D., Lawrenson, I.J., Sparke, C.H.S., 1975. The vapor pressure of naphthalene. J. Chem. Thermodyn. 7, 1173–1176.

Asako, Y., Faghri, M., 1987. Finite-volume solutions for laminar flow and heat transfer in a corrugated duct. J. Heat Transfer 109, 627–634.

Bhatti, M.S., Shah, R.K., 1987. Turbulent and transient flow convective heat transfer in ducts. In: Kakac, S., Shah, R.K., Aung, W. (Eds.), Handbook of Single-Phase Convective Heat Transfer. Wiley-Interscience, New York.

Cho, H.H., Rhee, D.H., 2001. Local heat/mass transfer measurement on the effusion plate in impingement/effusion cooling system. J. Turbomach. 123, 601–608.

Cho, H.H., Kim, Y.Y., Rhee, D.H., Lee, S.Y., Wu, S.J., Choi, C., 2003. The effects of gap position in discrete ribs on local heat/mass transfer in a square duct. J. Enhanced Heat Transfer 10 (3), 287–300.

Dittus, P.W., Boelter, M.K., 1985. Heat transfer in automobile radiators of the tubular type. Int. J. Heat Mass Transfer 7, 3–22.

Eckert, E.R.G., 1976. Analogies to heat transfer processes. In: Eckert, E.R.G., Goldstein, R.J. (Eds.), Measurements in Heat Transfer. Hemisphere Pub., New York, pp. 397–423.

Goldstein Jr., L., Sparrow, E.M., 1977. Heat/mass transfer characteristics for flow in a corrugated wall channel. J. Heat Transfer 99, 187–195.

Goldstein, R.J., Cho, H.H., 1995. A review of mass transfer measurements using naphthalene sublimation. Exp. Thermal Fluid Sci. 10, 416–434.

Islamoglu, Y., Parmaksizoglu, C., 2003. The effect of channel height on the enhanced heat transfer characteristics in a corrugated heat exchanger channel. Appl. Thermal Eng. 23, 979–987.

Islamoglu, Y., Parmaksizoglu, C., 2004. Numerical investigation of convective heat transfer and pressure drop in a corrugated heat exchanger channel. Appl. Thermal Eng. 24, 141–147.

Kline, S.J., McClintock, F., 1953. Describing uncertainty in single sample experiments. Mech. Eng. 75, 3–8.

McDonald, C.F., Wilson, D.G., 1996. The utilization of recuperated and regenerated engine cycles for high-efficiency gas turbines in the 21st century. Appl. Thermal Eng. 16 (8), 635–653.

Nishimura, T., Yano, K., Yoshino, T., Kawamura, Y., 1990. Occurrence and structure of Taylor–Görtler vortices induced in two-dimensional wavy channels for steady flow. J. Chem. Eng. Jpn. 23, 697–703.

O'Brien, J.E., Sparrow, E.M., 1982. Corrugated-duct heat transfer, pressure drop, and flow visualization. J. Heat Transfer 104, 410–416.

Rokni, M., Gatski, T.B., 2001. Predicting turbulent convective heat transfer in fully developed duct flows. Int. J. Heat Fluid Flow 22, 381–392.

Rokni, M., Sunden, B., 1998. 3D numerical investigation of turbulent forced convection in wavy ducts with trapezoidal cross-section. Int. J. Numer. Methods Heat Fluid Flow 8, 118–141.

Sawyers, D.R., Sen, M., Chang, H.C., 1998. Heat transfer enhancement in three-dimensional corrugated channel flow. Int. J. Heat Mass Transfer 41, 3559–3573.

Sparrow, E.M., Comb, J.W., 1983. Effect of interwall spacing and fluid flow inlet conditions on a corrugated-wall heat exchanger. Int. J. Heat/Mass Transfer 26 (7), 993–1005.

Utriainen, E., Sunden, B., 2000. Numerical analysis of a primary surface trapezoidal cross wavy duct. Int. J. Numer. Methods Heat Fluid Flow 6, 634–648.